# A paradigm for high-throughput screening of cell-selective surfaces coupling orthogonal gradients and machine learning-based cell recognition

Hongye Hao [a,b,1], Yunfan Xue [a,b,1], Yuhui Wu [a,b], Cong Wang [a,b], Yifeng Chen [a,b], Xingwang Wang [a,b], Peng Zhang [a,b,**], Jian Ji [a,b,*]

[a] MOE Key Laboratory of Macromolecule Synthesis and Functionalization, Department of Polymer Science and Engineering, Zhejiang University, Hangzhou, 310027, PR China
[b] International Research Center for X Polymers, International Campus, Zhejiang University, Haining, 314400, PR China

## A B S T R A C T

The combinational density of immobilized functional molecules on biomaterial surfaces directs cell behaviors. However, limited by the low efficiency of traditional low-throughput experimental methods, investigation and optimization of the combinational density remain daunting challenges. Herein, we report a high-throughput screening set-up to study biomaterial surface functionalization by integrating photo-controlled thiol-ene surface chemistry and machine learning-based label-free cell identification and statistics. Through such a strategy, a specific surface combinational density of polyethylene glycol (PEG) and arginine-glutamic acid-aspartic acid-valine peptide (REDV) leads to high endothelial cell (EC) selectivity against smooth muscle cell (SMC) was identified. The composition was translated as a coating formula to modify medical nickel-titanium alloy surfaces, which was then proved to improve EC competitiveness and induce endothelialization. This work provided a high-throughput method to investigate behaviors of co-cultured cells on biomaterial surfaces modified with combinatorial functional molecules.

## 1. Introduction

The ability to dictate cell behaviors and tissue regeneration is crucial for many biomedical devices [1–7]. For example, surface endothelialization is highly desired for many implantable cardiovascular devices, such as intravascular stents and artificial heart valves [8–10]. Co-grafting of multiple functional molecules could endow biomaterials with specialized properties to achieve complex biological goals [11–13]. While the spatial presentation and density of functional molecules largely determine cell responses [14], systematic quantitative studies on surface co-grafting remain challenging due to the difficulties associated with preparing and testing massive samples in orthogonal experiments [15–17].

High-throughput screening methods have been developed to investigate the interactions between cells and a vast number of biomaterials using highly integrated chips [18–23]. For example, miniaturized chips of polymer microarrays were used to study macrophage polarization and stem cell differentiation on the surfaces of biomaterials [24,25]. Compared with microarrays, chips with continuous gradients possess higher integration as every position along the gradients has unique properties [26]. Surfaces with chemical gradients are ideal for studying how the density of grafted molecules affects cell behaviors [14,27–29]. Furthermore, chips with orthogonal gradients formed by two independent gradients possess even higher integration and could be used to study the combinational effects of two different functional molecules on cell behaviors [30–32].

Despite the recent progress made in high-throughput experimental methods, the cumbersome manual data acquisition and analysis restrict the systematic study of biological effects on biomolecule co-grafted surfaces [17]. In addition, traditional cytological analysis always involves fluorescent labeling steps, which may increase the cost of the massive screening process, affect cell conditions, and impede real-time analysis [26]. Accordingly, the integration of an efficient, automatic, and low-cost method for cell characterization is essential for the

high-throughput screening process. Artificial intelligence has provided new solutions for efficient image processing and analysis [33]. Recently, our group has developed a machine learning-based image analysis method using combinational models to identify endothelial cells (ECs) and smooth muscle cells (SMCs) in a co-culture system [34]. The algorithm achieved automatic identification and statistics of co-cultured cells without any fluorescent labeling.

In this work, we developed a high-throughput workflow to screen the optimal surface combinational densities of two functional molecules to direct endothelialization by integrating chips with orthogonal gradients and machine learning-based automatic cell recognition (Fig. 1). Arginine-glutamic acid-aspartic acid-valine peptide (REDV) is a functional peptide that promotes the adhesion of ECs. In our previous study, we found that grafting REDV with a nonfouling polymer could enhance the preferential growth of ECs over SMCs on the surface through the synergistic action of the nonspecific resistance and specific cell interaction [12]. Herein, with the high-throughput setup, we were able to dig deeper into the phenomenon and found the optimal combinational densities of polyethylene glycol (PEG) and REDV. The surface modified with PEG and REDV at their optimal densities showed a high competitive coefficient of ECs over SMCs. **The composition was translated as a coating formula to** medical nickel-titanium alloy sheets, which showed excellent EC selectivity and induced endothelialization.

## 2. Results and discussion

### 2.1. Chips with orthogonal gradients

The chips with orthogonal gradients of two functional molecules can be considered material libraries with high integration. Thiol-terminated PEG and REDV were conjugated onto the surface of acrylated glass sides through thiol-ene chemistry. The orthogonal gradients were fabricated via a two-step reaction using light filter-controlled gradient ultraviolet (UV) irradiation. Specifically, surface acrylated glass slides (SA-slides) were fabricated by modifying glass slides (1 cm × 5 cm and 2 cm × 2 cm) with 3-Methacryloxypropyltrimethoxysilane (MEMO) (Fig. 2a). To find out the appropriate reaction condition to prepare the orthogonal gradients, a series of concentrations of the mono-thiolated PEG were reacted with SA-slides, and the conjugation densities were measured (Fig. S1). The results indicated that 5 mM of thiol-terminated molecules achieved the highest grafting amount by a short UV light irradiation (40 mW/cm$^2$, 15 s). To leave adequate acylate groups for the second reaction step, 2.5 mM PEG was used to modify the chip surface in the first reaction step. A light filter with gradient transmission (Fig. S2) was used to generate the first continuous gradient of PEG (Fig. 2b). The obtained samples were first characterized by water contact angle (WCA) measurement. As shown in Fig. 2c, the WCA of the surfaces decreased (from 73.5 ± 1.0 to 34.5 ± 0.9°) along the direction of the gradient, due to the increased PEG grafting density. To visualize the gradients, fluorescein isothiocyanate isomer labeled PEG (PEG-FITC) was mixed in the reaction solution before fabrication. As shown in Fig. S3a, the fluorescence intensity increased continuously along the gradient, consistent with the WCA result. The grafting density of PEG was calculated via a standard curve correlating the fluorescence intensity and PEG density (Fig. S3c), showing that the PEG density increased from 19.3 ± 3.0 to 55.5 ± 1.5 ng/cm$^2$ along the gradient (Fig. 2d). A chip with the REDV gradient was also fabricated and characterized, showing a similar trend with the PEG gradient (Fig. 2e, f, and Figs. S3b, d, f). X-ray photoelectron spectroscopy (XPS) was used to further characterize the REDV gradient. Five spots along the chip were chosen, and the grafting densities calculated using intensities from nitrogen atoms were consistent with that calculated with the fluorescent intensity (Fig. 2g and h, Table S1).

The chip with orthogonal gradients was fabricated on a 2 cm × 2 cm SA-slide via the two-step reaction (Fig. 3a). After the formation of the
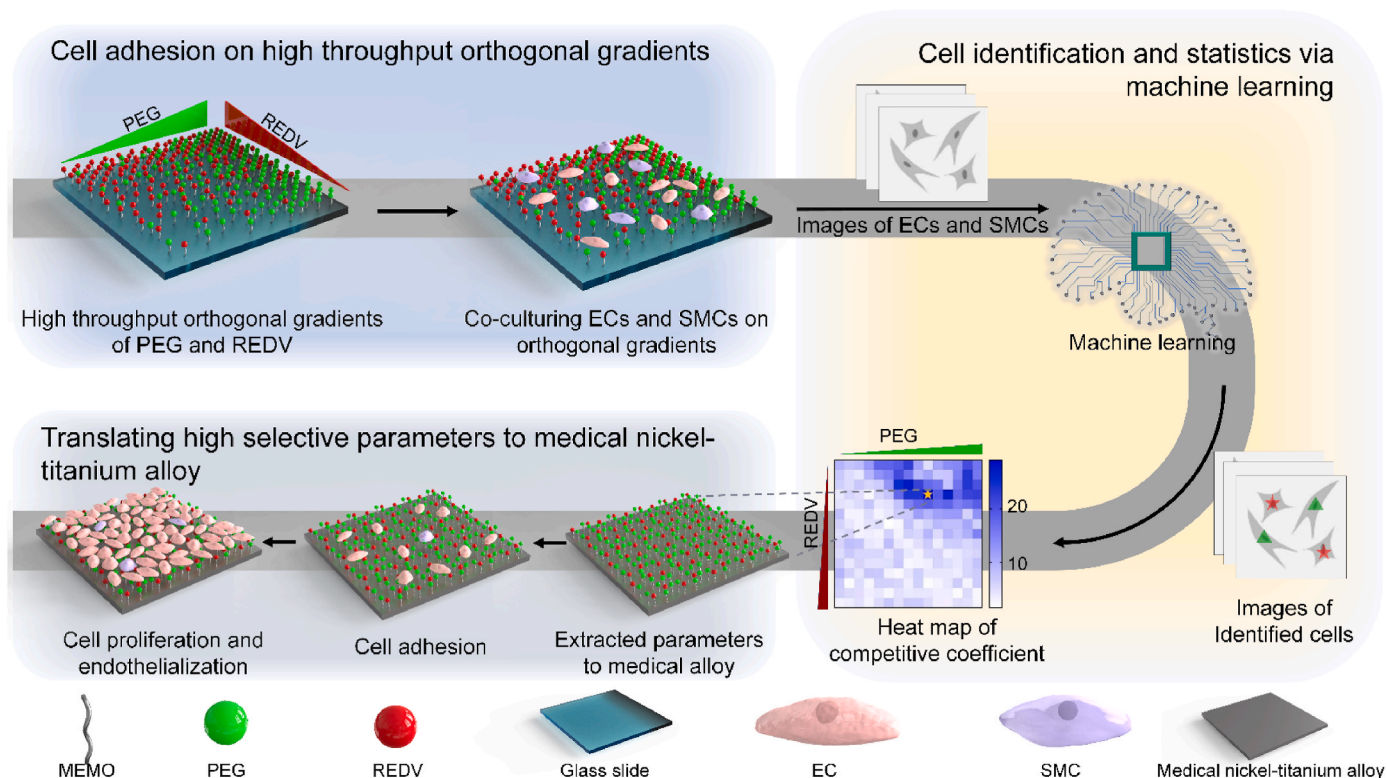


**Fig. 1.** Schematic illustration of the high-throughput workflow. For the rapid study of cell competitiveness induced by the combinational densities of surface co-grafted PEG and REDV, the chips with orthogonal gradients of PEG and REDV were fabricated on glass slides through thiol-ene chemistry. The adhered cells were then photographed and analyzed by a machine learning-based method to identify the optimal composition to induce endothelialization. Finally, the optimal composition was translated as a coating formula for implantable cardiovascular devices.
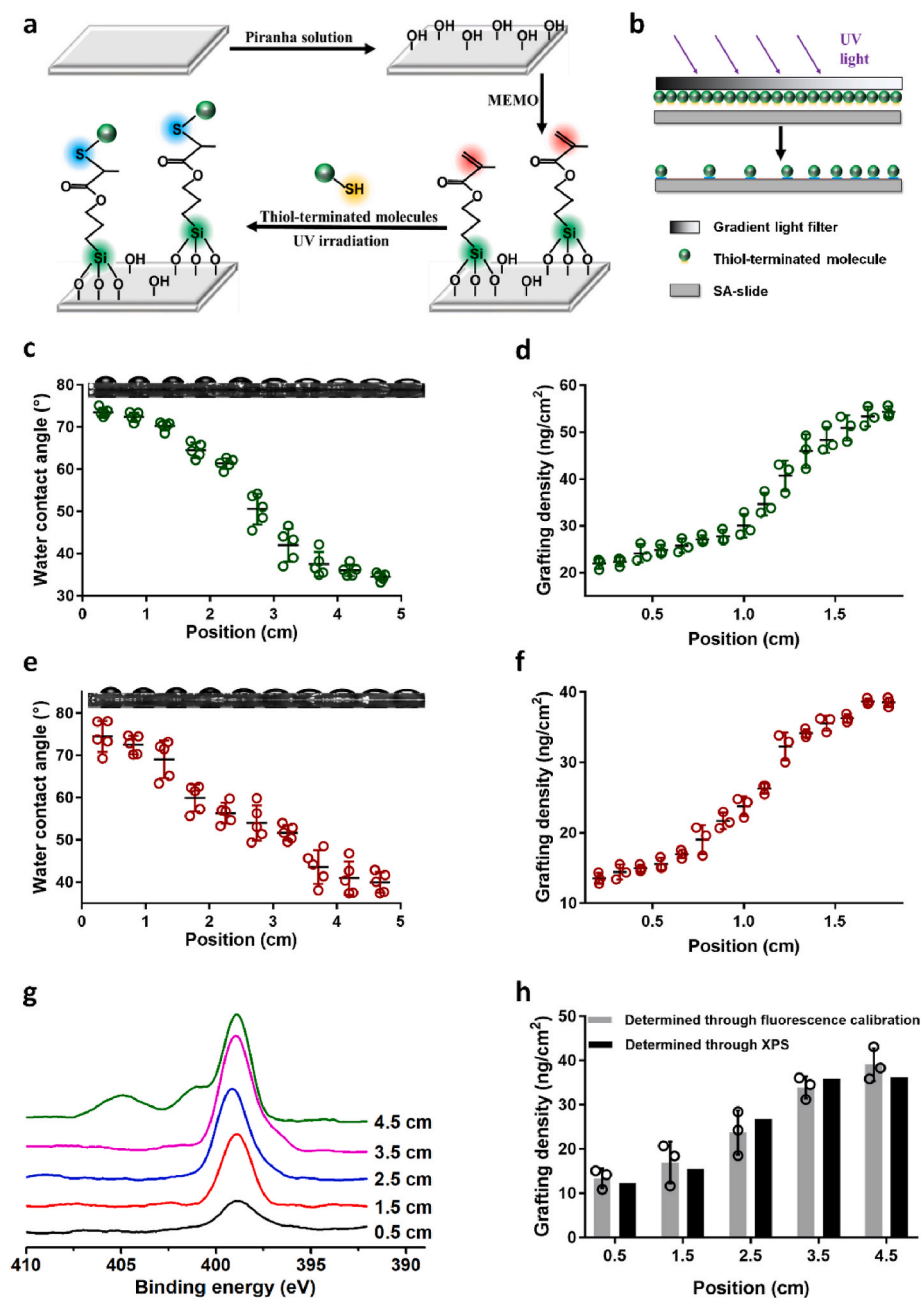
**Fig. 2.** Fabrication and characterization of the single gradients. Scheme of the **a)** surface modification approach and **b)** fabrication of continuous gradients. The **c)** water contact angle and **d)** PEG grafting density of the chip with a single PEG gradient. The **e)** water contact angle and **f)** REDV grafting density of the chip with a single REDV gradient. **g)** High-resolution N spectrums and **h)** grafting densities of 5 spots along the REDV gradient.

PEG gradient in one direction, the light filter was rotated for 90° to fabricate the REDV gradient in the orthogonal direction. The obtained surfaces were characterized by fluorescence intensity and WCA measurement. The chip showed orthogonal gradients with green color labeled PEG and red color labeled REDV (Fig. 3b, Fig. S4). Since both functional molecules increase the surface hydrophilicity, the WCAs decreased along the diagonal line (Fig. S5). As shown in Fig. 3c and d, the grafting density of PEG and REDV in the orthogonal gradients were determined through fluorescence calibration, and similar results were obtained compared with that of the single gradients (Fig. 2d, f).

### 2.2. Machine learning-based cell recognition

The chip with orthogonal gradients enables high-throughput testing of the cellular behaviors with combinational densities of PEG and REDV. When culturing cells on the chip, data can be easily collected using a microscope. However, in a co-culture system of ECs and SMCs, traditional methods to identify and count different types of cells from the image still need fluorescent labeling and semi-automatic statistics. To realize real high-throughput testing, we developed a label-free machine-learning method to automatically analyze the cells in the co-cultured system [34]. As shown in Fig. 4b, the machine learning workflow is composed of three steps. First, a modified UNet model (ResUNet) is used to predict binary images of cell nuclei based on brightfield images. Then, two unsupervised clustering algorithms of density-based spatial clustering of applications with noise (DBSCAN) and K-means are used to return the coordinates of each nucleus. Finally, single-cell images are segmented from the brightfield images based on the returned
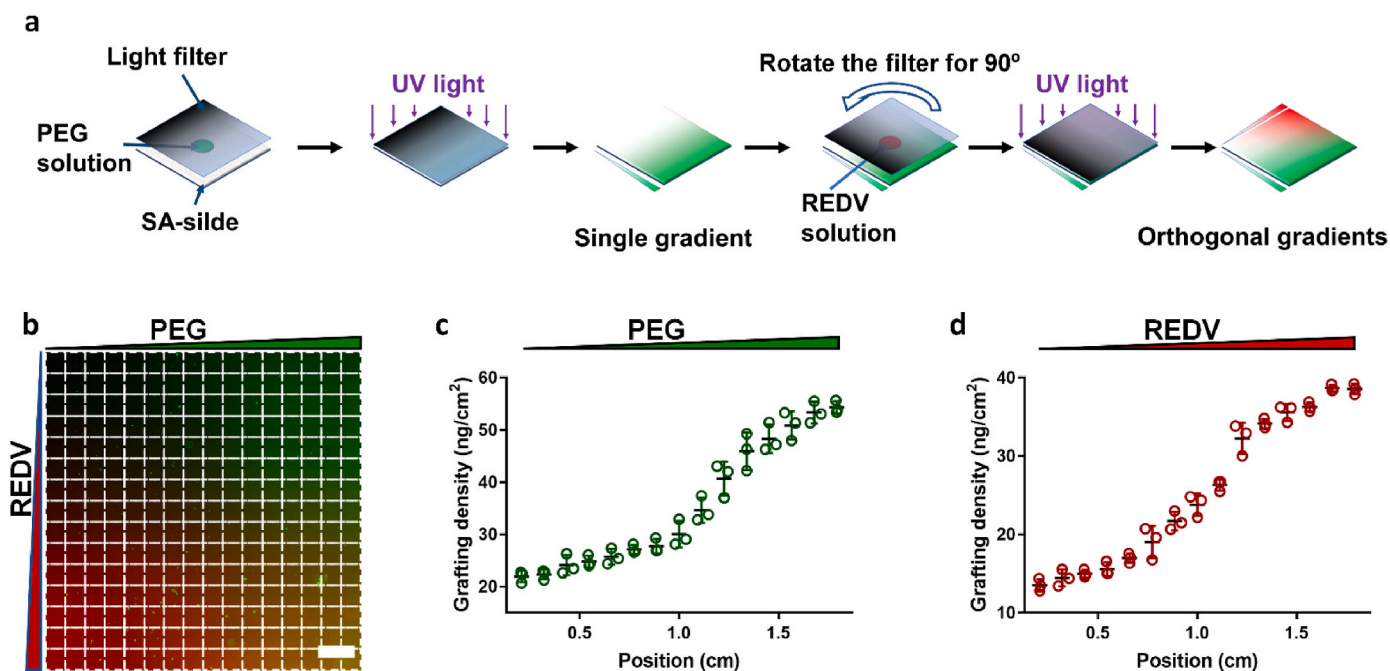
**Fig. 3.** Fabrication and characterization of the orthogonal gradients. a) Scheme of the fabrication process of the chip with orthogonal gradients. **b)** Fluorescent image (Scale bar: 2 mm) of the chip. PEG was labeled green and REDV was labeled red. Grafting densities of **c)** PEG and **d)** REDV along the two directions of the chip with orthogonal gradients.

coordinates and sent into a convolutional neural network with a skip connection (ResNet50V2) for classification. In this way, each cell in brightfield images can be located and identified. In the combinational method, the ResUNet and ResNet50V2 require supervised training before application. Considering that the PEG coating may affect cell morphology, we trained the models with cell images collected on single gradients of PEG and then applied the models to orthogonal gradient samples (Fig. 4a). The images were obtained under a microscope at the magnification of 100 × (Fig. 4c and d). On the testing set, ResNet50V2 achieved a classification accuracy of above 0.95 while ResUNet had a dice loss of 0.11 (Fig. 4e and f), suggesting the reliability of the models in analyzing the cell images. As the cell recognition was achieved by using brightfield images, the impacts of fluorescence labeling towards cell conditions were avoided, as a result, this method may also realize real-time monitoring for cell behaviors including adhesion, proliferation, and migration of different cell types in a co-culture system.

### 2.3. High-throughput screening of the combinational densities of PEG and REDV

With the established high-throughput experimental and data analytical methods, we used the workflow to study the effect of combinational densities of PEG and REDV on the cell competitiveness of ECs and SMCs. Equal amounts of ECs and SMCs were seeded on the orthogonal gradient chips (SA-slides were used as controls). After co-cultured for 4 h, stitched large images of the cells were acquired using automatic scanning of a microscope. The picture was further divided into 255 subareas (15 × 15) by a python script as the inputs of the machine learning models. The models then output the marked images (Fig. 5a and b) and quantitative data of EC and SMC counting in each subarea (Fig. 5c). To prove the correctness of the machine learning method, we also manually counted the cell numbers in five randomly selected areas after the cells were fluorescently labeled. As presented in Fig. S7, the cell adhesion densities obtained with these two approaches were consistent, suggesting the reliability of the cell identification and counting results from the machine learning method.

The cell counting results of the whole chip were shown in Fig. 5.

Along the gradient of REDV, the attachment of both types of cells increased as the peptide promotes adhesion by binding with integrin $\alpha 4 \beta 1$ [35]. On the other hand, the cell attachments were more sensitive to PEG densities in the low REDV density region, suggesting that the specific interaction between REDV and cell surface outperformed the nonspecific resistance from grafted PEG. Along the PEG gradient, the cell attachments first decreased as the PEG density increased. When the PEG density is greater than 50 ng/cm$^2$, the cell attachment numbers recovered to some extent, possibly due to the exhibited hydrophobicity caused by the assembling of the terminal methoxy groups [36].

The screening results showed that the combination of non-specific antifouling PEG and specific recognizing REDV peptide leads to cell selectivity in some but not all areas on the chip, indicating the importance of the combinational density of the two functional molecules (Fig. 5e). By contrast, the EC density is slightly lower than SMC density on the ungrafted SA-slides with a competitive coefficient of −0.13, suggesting no EC selectivity (area α in Fig. 5c, marked with red dashed frames in Fig. 5c–e). As shown in Fig. 5c, f, g, and Fig. S8, we selected and compared the cell adhesion on 3 areas with extreme characteristics including area β (high PEG density but low REDV density), area γ (low PEG density but high REDV density), and area δ (high densities of both PEG and REDV), with that of the ungrafted control slide. Although the area β showed a moderate cell selectivity with a competitive coefficient of 16.1, the attached EC number is low due to the nonspecific resistance to cell adhesion from the PEG molecules. The area γ and δ showed similar cell adhesion behavior regardless of the difference in PEG densities, showing weak cell selectivities with the high REDV grafting density.

The highest competitive coefficient on the chip appeared in area ε (marked with orange dashed frames in Fig. 5c–e), with a moderate PEG density of 40.7 ng/cm$^2$ and a low REDV density of 15.6 ng/cm$^2$. To understand the key factors affecting the competitive coefficients, we further analyzed the cell attachments on a series of areas that have similar density ratios of PEG/REDV (molar ratio 1.52–1.72) with that of the area ε (Fig. 5d, h-m). The results showed that both the ECs and SMCs attached more on the surface with increased densities of the immobilized molecules. Although the molar ratio of these two molecules kept
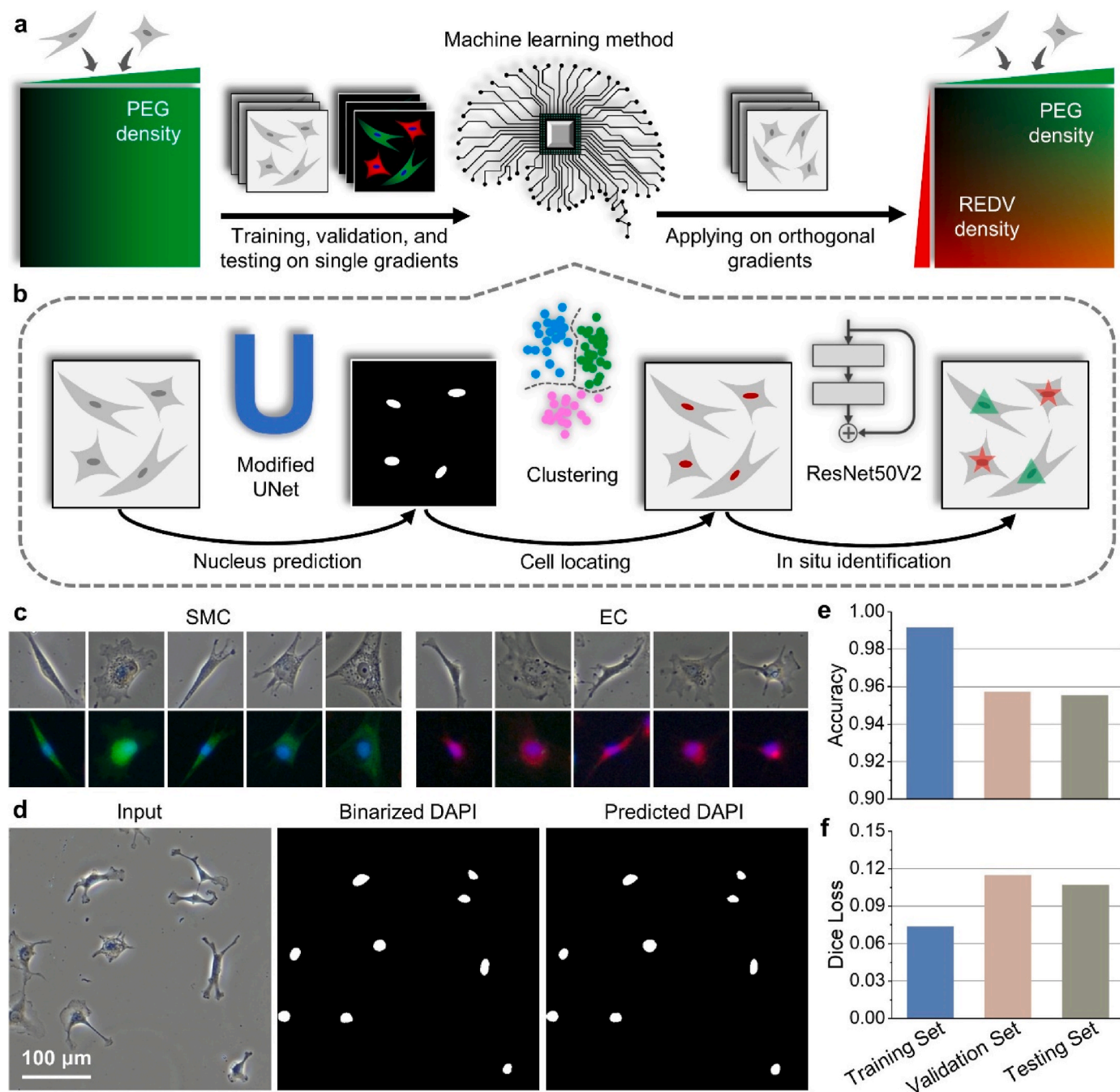
**Fig. 4.** Machine learning-based label-free cell analysis. a) Schematic illustration of the process. To obtain the training dataset for the machine learning models, cells were cultured on a chip with a single PEG gradient. Strictly paired brightfield images and fluorescent images (100 ×) of the cells were collected for the training, validation, and testing of the models. When analyzing co-cultured cells using the trained models, only brightfield images (100 ×) were collected and used for the identification and statistics of cells. **b)** Schematic illustration of the label-free cell analysis process of the machine learning methods. **c)** Representative cell images obtained on the chip with PEG gradient used for model testing. **d)** A representative image in the testing set for ResUNet. Left: brightfield image; middle: binarized fluorescent image with DAPI labeling; right: the model predicted image. The **e)** classification accuracy and **f)** dice loss of ResNet50V2 on the training, validation, and testing sets.

the same, the competitive coefficient first showed an upward trend to reach the peak, and then dropped quickly when the densities increased. The ratio of two different functional molecules immobilized on a biomaterial surface was often considered the key factor to determine cell behavior at the interface [14]. However, our results showed that the absolute density of the functional molecules in a co-grafting system also plays a key role to determine the biological effects at the material interface. With our high-throughput screening approach, the optimal combinational densities of immobilized PEG and REDV were efficiently identified to maximize the cell-selective function.

### 2.4. Validation on macro-surfaces

We identified the optimal combinational densities of the PEG/REDV on the chip with continuous orthogonal gradients. However, the cell adhesion on a micro-surface on the chip might be affected by its neighboring areas. The next question needs to be answered is that whether such combinational densities exhibit the same biological
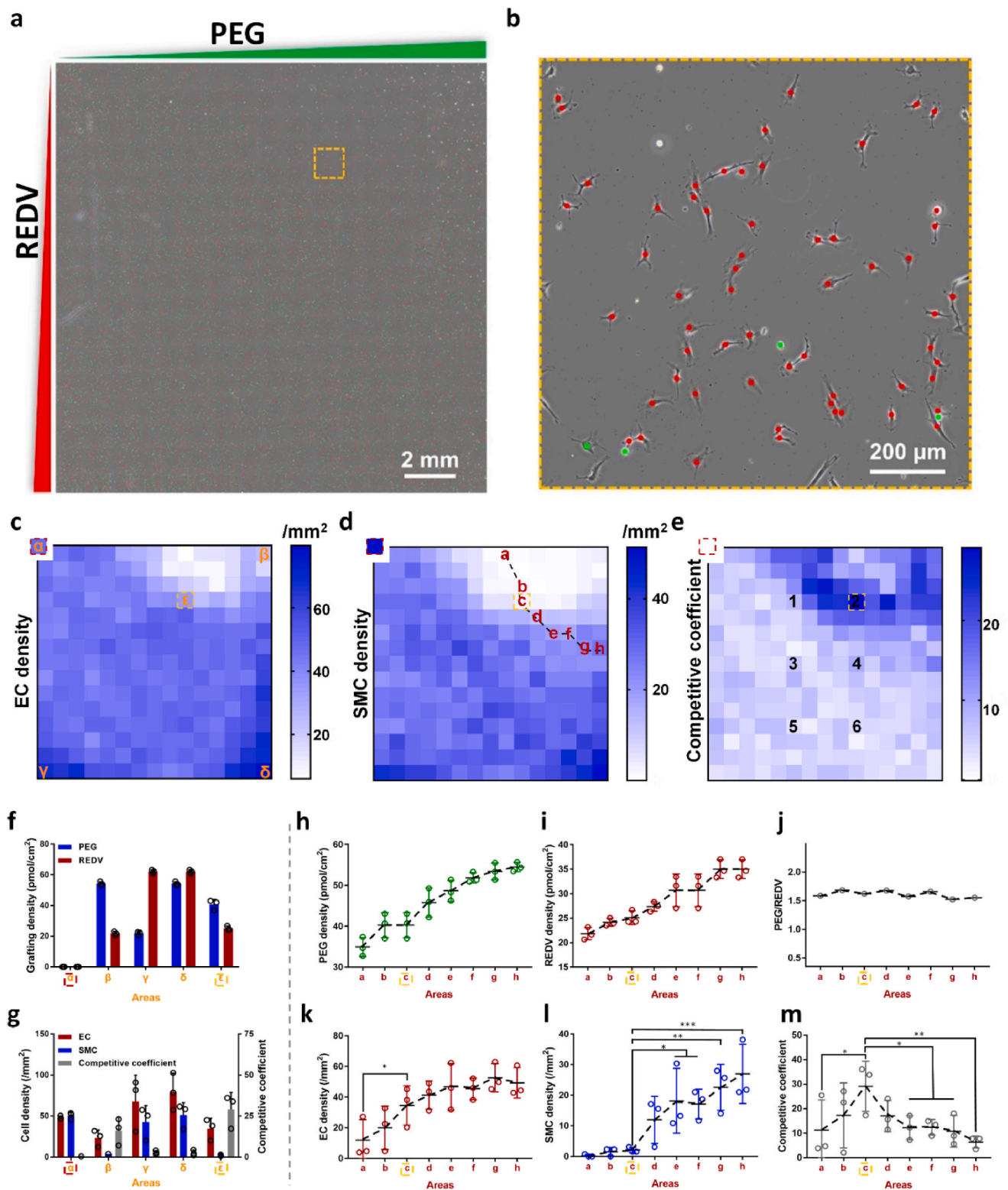
**Fig. 5.** Screening of the combinational densities of PEG/REDV on the chip with the orthogonal gradients. a) The processed image of the co-cultured cells on the chip. A bright field image of the cells was taken and processed by the machine learning-based label-free cell analysis to identify and count the cells. ECs are shown in red, and SMCs are shown in green. **b)** Zoomed-in image of the area in the orange dashed frame. Heat maps showing **c)** the EC density, **d)** the SMC density, and **e)** the competitive coefficient obtained by the machine learning-based analysis. The heat maps were obtained from three independent samples. The area in the upper left corner within the red dashed frame shows the EC density, the SMC density, and the competitive coefficient obtained from the SA-slide with no gradient. The orange dashed frame highlights the spot with the highest competitive coefficient. The **f)** grafting densities of PEG and REDV and **g)** the corresponding cell densities and competitive coefficients of the labeled areas in panel c (The results of significant difference analysis were shown in Fig. S8). The **h)** PEG grafting densities, **i)** REDV grafting densities, **j)** PEG/REDV ratios, **k)** EC densities, **l)** SMC densities, and **m)** competitive coefficients of the 8 marked areas in panel d. These areas have similar PEG/REDV ratios with the area that has the highest competitive coefficient (area c). Statistical significance was assessed with the analysis of variance test, *$p < 0.05$, **$p < 0.01$, ***$p < 0.001$. $p < 0.05$ denotes significant difference.

function on an independent large surface as that on the chip. To this end, 6 areas (as marked in Fig. 5e) including the one with the highest competitive coefficient (area 2) were chosen from the orthogonal gradients and translated to 2 cm × 2 cm large surfaces. The samples were prepared using light filters with homogeneous transmittances and characterized by the WCA test and fluorescence imaging. As shown in Fig. 6a, b and S8, the large surfaces showed the same combinational densities of the two molecules and WCAs as their corresponding areas on the chip. In the co-culture test, the attachments of ECs and SMCs showed similar results on the large surfaces as that on the micro-surfaces (Fig. 6c, d and S9), demonstrating that the combinational densities obtained from the continuous orthogonal gradients were also valid on large, homogeneous samples.

## 2.5. Translating to nickel-titanium alloy surfaces

The ultimate objective of improving EC competitiveness against SMC is to induce fast endothelialization on blood-contacting biomaterial implantations. Successful translation of the optimal combinational densities from the high throughput screening to a surface coating formula for materials used in clinical applications is crucial. To this end, medical-grade nickel-titanium alloy sheets were used as exemplary substrates and grafted with PEG and REDV under optimal modification conditions. Cell adhesion and proliferation were studied on the obtained samples using untreated nickel-titanium alloy sheets (Ut-sheets) as controls. As shown in Fig. 7a, b, a considerable amount of both ECs and SMCs adhered on the Ut-sheets, while PEG and REDV modified sheets (P&R-sheets) only supported EC adhesion with excellent EC selectivity. After 3 days of culture, the existence of a large number of SMCs astricted ECs to limited areas and hindered the formation of homogeneous endothelium on Ut-sheets. By contrast, integral endothelium was formed on P&R-sheets. The cell proliferation was also studied on acrylate modified medical nickel-titanium alloy sheets, showing similar results as the Ut-sheets (Fig. S11).

The integrity of the formed EC monolayers was further characterized by staining CD31 (platelet endothelial cell adhesion molecule-1, red), vWF (von Willebrand Factor, green) and cell nuclei (blue) (Fig. 7c). After 3 days of co-culture, the EC layers showed an island morphology that was surrounded by large areas of SMC layers on Ut-sheets. By contrast, ECs formed relatively integrated monolayers on the coated P&R-sheets with continuous surface expression of vWF and CD31, suggesting successful endothelialization. Vascular endothelium produces multiple vasoconstrictive and vasodilatory substances with anticoagulant or antithrombotic functions to maintain vascular homeostasis [37, 38]. To evaluate the function of EC monolayers formed on P&R-sheets, the expressions of tissue-type plasminogen activator (tPA), prostacyclin (PGI-2), and nitric oxide (NO), were characterized. As shown in Fig. 7d, the EC monolayers formed on P&R-sheets showed significantly higher expressions of tPA, PGI-2, and NO than that on the Ut-sheets, respectively. The P&R-sheets supported ECs to form integrated monolayers with biological functions, which is highly desired for the implantable cardiovascular devices. These results indicate the successful translation of the optimal combinational densities of PEG/REDV to a coating formula for implantable biomaterials.

## 3. Conclusion

In summary, we built a high-throughput workflow by integrating orthogonal gradient chips with the machine learning-based cellular analysis for systematic study of the biological effects of surface co-grafted functional molecules. With this setup, the effects of the combinational densities of PEG and REDV on cell competitiveness in the EC/
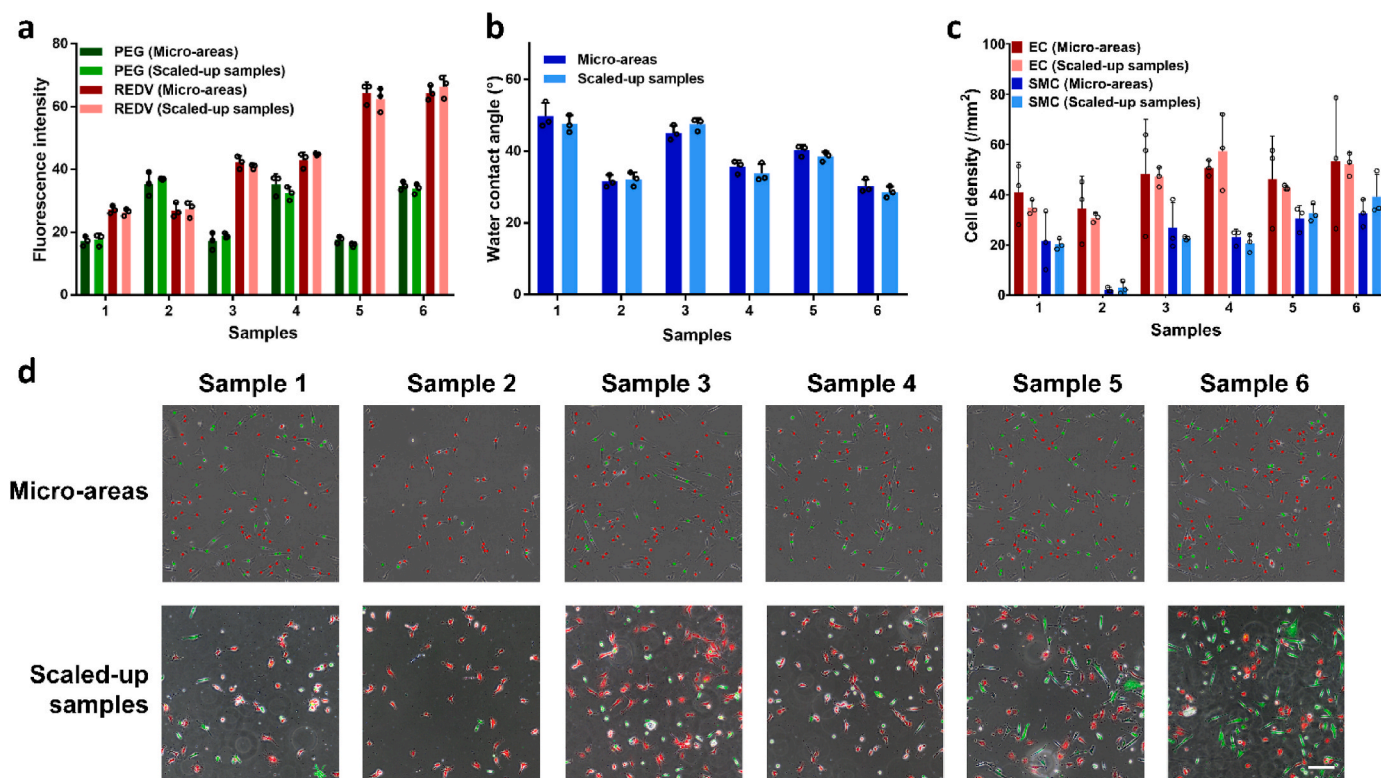


**Fig. 6.** Validation of the combinational densities of PEG/REDV on scaled-up surfaces. The comparison of **a)** fluorescent intensities and **b)** WCAs of the micro-areas (1–6 in Fig. 5e) from the chip and the corresponding scaled-up samples. The statistics **c)** and **d)** photographs of co-cultured ECs and SMCs on the micro-areas of the chip and the scaled-up samples (Scale bar: 0.2 mm, the original photo is shown in Fig. S10). Statistical significance was assessed with the analysis of variance test, a probability value of p < 0.05 is considered significant, and no statistical significance was found between all results (including fluorescence intensity, WCA, and cell density) when comparing the micro-areas and the corresponding scaled-up samples.
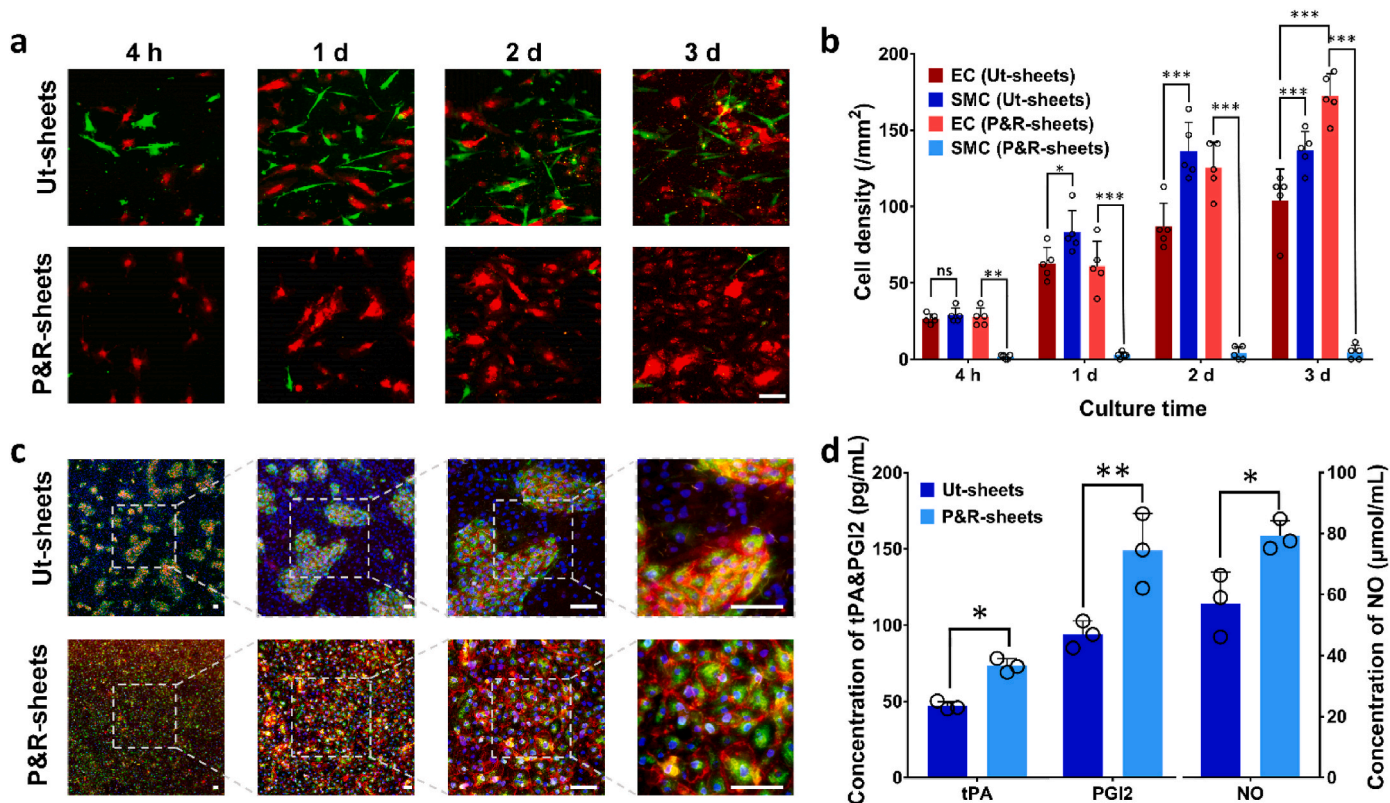
**Fig. 7.** Endothelialization on the coated nickel-titanium alloy surfaces. a) Photographs and **b)** the corresponding cell densities of ECs and SMCs on Ut-sheets and P&R-sheets after different culture times (Scale bar: 0.1 mm, the original photo is shown in Fig. S12). Pre-stained ECs and SMCs were seeded on the samples, and photographed after certain periods (4 h for adhesion, 1–3 days for proliferation). **c)** The morphology of cell monolayers formed on Ut-sheets and P&R-sheets. The ECs were stained for CD31 (green), and vWF (red) and both ECs and SMCs were stained for nuclei (blue) (Scale bars: 0.1 mm, the original photo is shown in Fig. S13). **d)** The concentrations of tPA, PGI-2, and NO released in the culture media from ECs grown on the Ut-sheets and P&R-sheets. Statistical significance was assessed with the analysis of variance test, *$p < 0.05$; **$p < 0.01$; ***$p < 0.001$; ns means not significant. $p < 0.05$ denotes significant difference.

SMC co-culture was studied, and an optimal composition was identified to induce the highest EC selectivity. The biological effects of the compositions found through the orthogonal gradients were successfully validated on independent large surfaces. In addition, the optimal composition was translated as a surface coating formula for implantable cardiovascular devices. The workflow provided an efficient way for high-throughput study and screening of the biological effects mediated by the combinations of different surface immobilized functional molecules.

## 4. Methods

**Materials.** Thiol terminated mPEG (liner, M$w$ = 1000) and Fluorescein isothiocyanate isomer labeled Mono-thiolated mPEG (PEG-FITC, the molecular weight of PEG was 1000) were purchased from Seebio Biotech (Shanghai) Co., Ltd. 3-Methacryloxypropyltrimethoxysilane (MEMO, 95%) was purchased from J&K Scientific. Irgacure2959 (I2959, 2-Hydroxy-4'-(2- Hydroxyethoxy)-2-methylpropiophenone) was purchased from Sigma-Aldrich. Ethanol, 2-Hydroxy-1-ethanethiol, toluene, sulphuric acid (98%), and hydrogen peroxide (30%) were purchased from China Pharmaceutical Group Chemical Reagents Co., Ltd. ʟ-Cysteine-arginine-glutamic acid-aspartic acid-valine peptide (REDV) and carboxytetramethylrhodamine labeled ʟ-Cysteine-arginine-glutamic acid-aspartic acid-valine peptide (REDV-TRAMA) were purchased from NJPeptide, China. Light filters with light transmittance gradient or constant light transmittance were designed using AutoCAD and fabricated by Beijing Daheng Photoelectric Technology Company. The water used in this work was purified by the Milli-Q system (Millipore, USA).

**Fabrication of surface acrylated substrate.** Glass slides were washed with water 3 times and immersed in piranha solution ($H_2SO_4$: $H_2O_2$ = 7:3; v/v) for 15 min. Then, they were washed repeatedly with water 3 times and dried with nitrogen. Next, they were immersed in the MEMO solution (0.5 vol% in toluene) for 8 h. Finally, the samples were washed with toluene, ethanol, and water 2 times, respectively, and dried under 37 °C. For the fabrication of MEMO-modified medical nickel-titanium alloy sheets, the sheets were washed with water and ethanol 3 times, respectively, dried with nitrogen, and treated with plasma. Then the sheets were treated with MEMO solution, washed, and dried in the same way described above.

**Fabrication of gradients and scaled-up samples.** Aqueous reaction solutions of I2959 (0.05 wt%) and PEG (or REDV, 2.5 mM) were prepared using distilled water. To create single gradients, 12.5 μL/cm$^2$ of the reaction solution was pipetted onto an SA-slide, and an equal-sized light filter with a light transmittance gradient was placed on top of the solution to form a thin layer in contact with the glass slide, the slide was then exposed to UV light (40 mW/cm$^2$) for 15 s, washed with water 5 times to remove unbound PEG (or REDV), and dried with nitrogen. To create orthogonal gradients, after creating an initial PEG gradient, the slide was covered by the reaction solution of REDV and I2959 and exposed to UV light in the same condition with the light filter rotated for 90°. For the fabrication of scaled-up samples, light filters possessing constant light transmittance were used instead of that with light transmittance gradients. Medical nickel-titanium alloy sheets modified with PEG and REDV were fabricated in the same way, with MEMO-modified medical nickel-titanium alloy sheets used instead of SA-slides.

**Surface characterization.** The water contact angle of the samples

was carried out with a contact angle measurement (Kruss DSA 100). 5 μL distilled water was applied with a syringe needle to the sample. The values quoted are the average of five measurements on parallel samples.

To characterize the presence of single and orthogonal gradients by fluorescence intensity, PEG containing 2 mol% PEG-FITC and REDV containing 2 mol% REDV-TRAMA were used to fabricate the gradients. Fluorescent photographs were taken using a fluorescence microscope (Nikon intensilight C-HGFI) and merged using NIS-Elements AR software for orthogonal gradients. The fluorescent photographs of gradients were divided equally into certain parts along the gradients (for single gradients, the fluorescent photographs were divided equally into 10 parts, while for orthogonal gradients, 1.5 mm of edges was firstly removed for fluorescent photographs of each channel, the rest part was then divided equally into 15 parts), and the mean intensity for each part was computed and averaged using ImageJ software. The values quoted are the average of three measurements on parallel samples. For the calculation of grafting density, aqueous solutions of different concentrations of PEG (containing 2 mol% PEG-FITC or REDV containing 2 mol % REDV-TRAMA) were pipetted onto SA-slide and dried to form spots with different PEG (or REDV) density. After fluorescence imaging, the fluorescence intensity of the spots was computed and averaged using ImageJ software (the values quoted are the average of five measurements on parallel samples), a standard calibration curve of fluorescence intensity and density was then obtained and used to calculate the grafting densities of gradient samples.

XPS data were obtained with a Thermo Scientific ESCALAB 250Xi equipped with an Al Ka X-ray source (1486.6 eV). All spectra were collected at a take-off angle of 30° to the surface of the sample. 5 points on the REDV gradient were characterized, the corresponding grafting densities were calculated with the theoretical density of MEMO (465 pmol/cm$^2$) [31,39–42], the ratio of C/N ($R_{C/N}$) from XPS data, and the molecular formula of REDV ($C_{23}N_8H_{40}O_{10}S$) and MEMO ($C_{10}H_{20}O_5Si$) by using the following formula:

$$REDV\ density = \frac{10}{8R_{C/N} - 23} \times 465\ pmol\Big/cm^2$$

**Cell isolation and culture.** Human primary umbilical vein endothelial cells (ECs) and human primary umbilical artery smooth muscle cells (SMCs) were isolated freshly from human umbilical veins and arteries after approval by the local medical ethics committee and used for experiments between 3 and 8 passages.

ECs were cultured in EC medium supplemented with 10% fetal bovine serum, 20 mg/mL ECGF, and 1% UI/mL streptomycin-penicillin in a culture dish at 37 °C and 5% CO$_2$. SMCs were cultured in SMC medium supplemented with 10% fetal bovine serum and 1% UI/mL streptomycin-penicillin in a culture dish at 37 °C and 5% CO$_2$. The culture medium was changed every 3 days and culture dishes with 80–90% confluence were used for further cell experiments.

**Cell adhesion.** Before cell seeding, All samples were immersed in aqueous reaction solutions of I2959 (0.05 wt%) and 2-Hydroxy-1-ethanethiol (0.3 vol%) and exposed to UV light (40 mW/cm$^2$) for 10 min, and washed with water 5 times. ECs and SMCs were stained by adding CellTracker™ Orange CMTMR (5-(and-6)-(((4chloromethyl)benzoyl) amino)tetramethylrhodamine) (1 μg/mL) and CellTracker™ Green CMFDA (5-chloromethylfluorescein diacetate) (1 μg/mL), respectively, for 30 min. Then both ECs and SMCs were detached, resuspended in EC medium with 20 mg/mL ECGF and 1% UI/mL streptomycin-penicillin, mixed in a 1:1 ratio, seeded on samples in 6-well plates with a cell density of 10000 cells/cm$^2$ (5000 cells/cm$^2$ for each type of cells), and incubated for 4 h. Finally, the cells were fixed with paraformaldehyde and fluorescently photographed using a fluorescence microscope (Nikon intensilight C-HGFI).

**Image preprocessing and machine learning models.** An inverted microscope (ECLIPSE Ti2, Nikon, Japan) was used to capture all the images in our study in a phase contrast channel or a fluorescent channel.

In the training and testing stage, large images of 100 × collected from PEG gradients were directly cut into smaller images of 512 × 512 px$^2$ for ResUNet. Single cell images (128 × 128 px$^2$) for ResNet50V2 were also cut from large images according to the locations of cell nuclei returned by clustering algorithms applied on fluorescent channel. Training sets, validation sets, and testing sets were randomly divided at the ratio of 8:1:1. Specific numbers of image in each set were presented in Table S2.

Please see our previous publication [34] for the detailed model architectures and design of the method. For the training of ResUNet, the binary training labels were obtained from the original DAPI channel by calling cv2.adaptiveThreshold. An adam optimizer was used to minimize the dice loss between the binary labels and predictions. The training went for 40 epochs with a batch size of 2. The model achieved the lowest loss on the validation set was saved for testing and application on orthogonal gradients. The low-bound parameter in the clustering step to leave out noises was reduced to 50 (100 in our previous study) considering the lower magnification of images here. For the training of ResNet50V2, an SGD optimizer with momentum of 0.9 was used to minimize the categorical cross entropy. The initial learning rate was set as 0.0001 and set to decrease 50% per 15 epochs. The training went for 60 epochs with a batch size of 32. The model achieved the highest accuracy on the validation set was saved for testing and application on orthogonal gradients. At the application stage, the input size of ResUNet was adjusted to 1536 × 1536 px$^2$ which is close to an independently captured normal image using our microscope (1608 × 1608 px$^2$). 255 subareas were separately put into models for prediction. The 255 output images with markers were then stitched to a large one using a python script. The method can at the same time return an excel file containing all the predicted numbers of EC and SMC in each subarea.

**Competitive coefficient.** The competitive coefficient is expected to reflect the adhesion advantage of EC over SMC and the absolute cell density at the same time. It should meet two requirements. First, it increases with the density of EC and decreases with the density of SMC. Second, it should avoid the situation that 0 is divisor as what will happen when simply using the ratio of two cells as the index. Accordingly, it is defined as below, where EC and SMC are the densities (/mm$^2$) of the two cells.

$$Competitive\ Coefficient = (EC - SMC)\delta^{-SMC}$$

(EC-SMC) reflects the adhesion advantage of EC over SMC, while $\delta^{-SMC}$ is a penalty term reflecting the absolute density of SMC. δ is a constant used to control the change rate of the penalty term. Because SMC was under 60/mm$^2$ in our study, δ was set as 1.05. The curve of penalty term as a function of SMC density was presented in Fig. S14.

**Cell Proliferation.** ECs and SMCs were stained, detached, resuspended, and mixed in the same way for cell adhesion as described above, and seeded on samples in 6-well plates with a cell density of 10000 cells/cm$^2$ (5000 cells/cm$^2$ for each type of cells). After certain incubation time (4 h, 1 day, 2 days, and 3 days), the cells were fixed with paraformaldehyde and fluorescently photographed using a fluorescence microscope (Nikon intensilight C-HGFI). Cells on each slide were counted manually. The values quoted are the average of five measurements on parallel samples.

**Characterization of EC Monolayer.** ECs and SMCs suspension in EC medium with 20 mg/mL ECGF and 1% UI/mL streptomycin-penicillin were mixed in a 1:1 ratio and seeded on samples in 6-well plates with a cell density of 20000 cells/cm$^2$ (10000 cells/cm$^2$ for each type of cells). After 3 d culture, the cells were fixed with paraformaldehyde and treated with 0.1% Triton X-100. Cell staining was performed for nuclei (1:100, DAPI, Sigma), von Willebrand factor (anti-vWF-FITC, Invitrogen), and CD31 (anti-CD31-red, Sigma). Images were obtained using fluorescence microscope (Nikon intensilight C-HGFI).

To measure the expression of NO, PGI-2, and tPA by EC monolayer, the culture medium was changed after 2 d culture, then collected after 24 h, and measured by NO assay kit, human PGI-2 kit, and human TPA

ELISA kit (Feiyubio, China).

**Statistical analysis.** Statistical significance was assessed with ANOVA test and a probability value of $p < 0.05$ is considered significant: $*P < 0.05$, $**P < 0.01$, $***P < 0.001$. The error bars represent standard deviation of the mean value of each type of experiments.

### Ethics approval and consent to participate

This study does not perform any experiments on animals. All performed examinations and samples collection did not require local ethics committee approval.

### Declarations of competing interest

The authors declare that they have no financial and personal relationships with other people or organizations that could have appeared to influence the work reported in this paper.

### CRediT authorship contribution statement

**Hongye Hao:** Conceptualization, Methodology, Validation, Formal analysis, Investigation, Writing – original draft, Writing – review & editing, Visualization, Funding acquisition. **Yunfan Xue:** Conceptualization, Methodology, Validation, Formal analysis, Investigation, Data curation, Writing – original draft, Writing – review & editing, Visualization. **Yuhui Wu:** Methodology, Writing – original draft. **Cong Wang:** Investigation. **Yifeng Chen:** Methodology. **Xingwang Wang:** Methodology. **Peng Zhang:** Conceptualization, Supervision, Writing – review & editing. **Jian Ji:** Conceptualization, Supervision, Funding acquisition, Project administration, Writing – review & editing.

### Acknowledgements

### Appendix A. Supplementary data

Supplementary data to this article can be found online at https://doi.org/10.1016/j.bioactmat.2023.04.022.

### References

[1] S. Garg, P.W. Serruys, Coronary stents, J. Am. Coll. Cardiol. 56 (2010) S43–S78.
[2] X. Zhang, W. Jiang, C. Xie, X. Wu, Q. Ren, F. Wang, X. Shen, Y. Hong, H. Wu, Y. Liao, Y. Zhang, R. Liang, W. Sun, Y. Gu, T. Zhang, Y. Chen, W. Wei, S. Zhang, W. Zou, H. Ouyang, Msx1+ stem cells recruited by bioactive tissue engineering graft for bone regeneration, Nat. Commun. 13 (2022) 5211.
[3] C.-Y. Lin, Y.-L. Wang, Y.-J. Chen, C.-T. Ho, Y.-H. Chi, L.Y. Chan, G.-W. Chen, H.-C. Hsu, D.W. Hwang, H.-C. Wu, S.-C. Hung, Collagen-binding peptides for the enhanced imaging, lubrication and regeneration of osteoarthritic articular cartilage, Nat. Biomed. Eng. 6 (2022) 1105–1117.
[4] H. Liu, Y. Du, J.-P. St-Pierre, M.S. Bergholt, H. Autefage, J. Wang, M. Cai, G. Yang, M.M. Stevens, S. Zhang, Bioenergetic-active materials enhance tissue regeneration by modulating cellular metabolic state, Sci. Adv. 6 (2020), eaay7608.
[5] D. Henn, K. Chen, T. Fehlmann, A.A. Trotsyuk, D. Sivaraj, Z.N. Maan, C.A. Bonham, J.A. Barrera, C.J. Mays, A.H. Greco, S.E. Moortgat Illouz, J.Q. Lin, S.R. Steele, D. S. Foster, J. Padmanabhan, A. Momeni, D. Nguyen, D.C. Wan, U. Kneser, M. Januszyk, A. Keller, M.T. Longaker, G.C. Gurtner, Xenogeneic skin transplantation promotes angiogenesis and tissue regeneration through Vitamin D-Activated Trem2+ Macrophages, Sci. Adv. 7 (2021) eabi4528.
[6] D.D. Damian, K. Price, S. Arabagi, I. Berra, Z. Machaidze, S. Manjila, S. Shimada, A. Fabozzo, G. Arnal, D. Van Story, J.D. Goldsmith, A.T. Agoston, C. Kim, R. W. Jennings, P.D. Ngo, M. Manfredi, P.E. Dupont, In vivo tissue regeneration with robotic implants, Sci. Rob. 3 (2018), eaaq0018.
[7] F.B. a, T.A.M. B, K.D.G. A, C.A.V.B. A, Advanced biomaterials for skeletal tissue regeneration: instructive and smart functions - ScienceDirect, Mater. Sci. Eng. R Rep. 59 (2008) 38–71.
[8] R.J. Smith, B. Nasiri, J. Kann, D. Yergeau, J.E. Bard, D.D. Swartz, S.T. Andreadis, Endothelialization of arterial vascular grafts by circulating monocytes, Nat. Commun. 11 (2020) 1622.
[9] Y. Chen, P. Gao, L. Huang, X. Tan, N. Zhou, T. Yang, H. Qiu, X. Dai, S. Michael, Q. Tu, N. Huang, Z. Guo, J. Zhou, Z. Yang, H. Wu, A tough nitric oxide-eluting hydrogel coating suppresses neointimal hyperplasia on vascular stent, Nat. Commun. 12 (2021) 7079.
[10] F. Otsuka, A.V. Finn, S.K. Yazdani, M. Nakano, F.D. Kolodgie, R. Virmani, The importance of the endothelium in atherothrombosis and coronary stenting, Nat. Rev. Cardiol. 9 (2012) 439–453.
[11] Q. Chen, S. Yu, D. Zhang, W. Zhang, H. Zhang, J. Zou, Z. Mao, Y. Yuan, C. Gao, R. Liu, Impact of antifouling PEG layer on the performance of functional peptides in regulating cell behaviors, J. Appl. Comput. Sci. 141 (2019) 16772–16780.
[12] Y. Wei, Y. Ji, L.L. Xiao, Q.K. Lin, J.P. Xu, K.F. Ren, J. Ji, Surface engineering of cardiovascular stent with endothelial cell selectivity for in vivo re-endothelialisation, Biomaterials 34 (2013) 2588–2599.
[13] R. Zhou, Y. Wu, K. Chen, D. Zhang, Q. Chen, D. Zhang, Y. She, W. Zhang, L. Liu, Y. Zhu, C. Gao, R. Liu, A polymeric strategy empowering vascular cell selectivity and potential application superior to extracellular matrix peptides, Adv. Mater. 34 (2022), 2200464.
[14] Z. Fang, J. Chen, Y. Zhu, G. Hu, H. Xin, K. Guo, Q. Li, L. Xie, L. Wang, X. Shi, Y. Wang, C. Mao, High-throughput screening and rational design of biofunctionalized surfaces with optimized biocompatibility and antimicrobial activity, Nat. Commun. 12 (2021) 3757.
[15] A.D. Abreu-Rejon, W. Herrera-Kao, A. May-Pat, A. Avila-Ortega, N. Rodriguez-Fuentes, J.A. Uribe-Calderon, J.M. Cervantes-Uc, Effect of PEG grafting density on surface properties of polyurethane substrata and the viability of osteoblast and fibroblast cells, J. Mater. Sci. Mater. Med. 33 (2022) 45.
[16] C.S. Li, X.X. Li, Y. Liu, Y. Sun, Implications from the grafting density and ionic capacity effects on protein adsorption to poly (N,N-dimethylaminopropyl acrylamide)-grafted sepharose FF, Biochem. Eng. J. 157 (2020), 107546.
[17] H.Y. Hao, J.J. Huang, P. Liu, Y.F. Xue, J. Wang, F. Jia, K.F. Ren, Q. Jin, J. Ji, Rapid buildup arrays with orthogonal biochemistry gradients via light-induced thiol-ene "click" chemistry for high-throughput screening of peptide combinations, ACS Appl. Mater. Interfaces 12 (2020) 20243–20252.
[18] C.G.S. Jr, L.G. Sheng, Combinatorial and high-throughput screening of biomaterials, Adv. Mater. 23 (2011) 369–387.
[19] S. Ankam, B.K. Teo, M. Kukumberg, E.K. Yim, High throughput screening to investigate the interaction of stem cells with their extracellular microenvironment, Organogenesis 9 (2013) 128–142.
[20] M. Darnell, D.J. Mooney, Leveraging advances in biology to design biomaterials, Nat. Mater. 16 (2017) 1178–1185.
[21] X. Li, X. Yang, L. Liu, P. Zhou, J. Zhou, X. Shi, Y. Wang, A microarray platform designed for high-throughput screening the reaction conditions for the synthesis of micro/nanosized biomedical materials, Bioact. Mater. 5 (2020) 286–296.
[22] K. Zhou, Y. Li, L. Zhang, L. Jin, J. Pei, Nano-micrometer surface roughness gradients reveal topographical influences on differentiating responses of vascular cells on biodegradable magnesium, Bioact. Mater. 6 (2021) 262–272.
[23] Y. Li, S. Wang, Y. Dong, P. Mu, Q. Huang, Effect of size and crystalline phase of TiO2 nanotubes on cell behaviors: a high throughput study using gradient TiO2 nanotubes, Bioact. Mater. 5 (2020) 1062–1070.
[24] H.M. Rostam, L.E. Fisher, A.L. Hook, D.A. Winkler, L. Kmmerling, Immune-instructive polymers control macrophage phenotype and modulate the foreign body response in vivo, Matter 2 (2020) 1564–1581.
[25] N. Brandenberg, S. Hoehnel, F. Kuttler, K. Homicsko, C. Ceroni, T. Ringel, N. Gjorevski, G. Schwank, G. Coukos, G. Turcatti, M.P. Lutolf, High-throughput automated organoid culture via stem-cell aggregation in microcavity arrays, Nat. Biomed. Eng. 4 (2020) 863–874.
[26] J. Yang, F.R.A.J. Rose, N. Gadegaard, M.R. Alexander, A high-throughput assay of cell-surface interactions using topographical and chemical gradients, Adv. Mater. 21 (2010) 300–304.
[27] N.D. Gallant, K.A. Lavery, E.J. Amis, M.L. Becker, Universal gradient substrates for "click" biofunctionalization, Adv. Mater. 19 (2010) 965–969.
[28] T. Ren, S. Yu, Z. Mao, S.E. Moya, L. Han, C. Gao, A complementary density gradient of poly(hydroxyethyl methacrylate) and YIGSR selectively guides migration of endotheliocytes, Biomacromolecules 15 (2014) 2256–2264.
[29] W. Luo, M.N. Yousaf, Tissue morphing control on dynamic gradient surfaces, J. Appl. Comput. Sci. 133 (2011) 10780–10783.
[30] Y. Ma, J. Zheng, E.F. Amond, C.M. Stafford, M.L. Becker, Facile fabrication of "dual click" one- and two-dimensional orthogonal peptide concentration gradients, Biomacromolecules 14 (2013) 665–671.
[31] Y. Ma, G.M. Policastro, Q. Li, J. Zheng, R. Jacquet, W.J. Landis, M.L. Becker, Concentration-Dependent hMSC differentiation on orthogonal concentration gradients of GRGDS and BMP-2 peptides, Biomacromolecules 17 (2016) 1486–1495.
[32] S.L. Vega, M.Y. Kwon, K.H. Song, C. Wang, R.L. Mauck, L. Han, J.A. Burdick, Combinatorial hydrogels with biochemical gradients for screening 3D cellular microenvironments, Nat. Commun. 9 (2018), e0188645.
[33] Y. Xue, H. Qian, X. Li, J. Wang, K. Ren, J. Ji, A deep-learning-based workflow to deal with the defocusing problem in high-throughput experiments, Bioact. Mater. 11 (2022) 218–229.

[34] Y. Xue, Y. He, J. Wang, K. Ren, P. Tian, J. Ji, Label-free and in situ identification of cells via combinational machine learning models, Small Methods 6 (2022), 2101405.

[35] S.P. Massia, J.A. Hubbell, Vascular endothelial cell adhesion and spreading promoted by the peptide REDV of the IIICS region of plasma fibronectin is mediated by integrin alpha 4 beta 1, J. Biol. Chem. 267 (1992) 14019–14026.

[36] L.D. Unsworth, H. Sheardown, J.L. Brash, Protein-resistant poly(ethylene oxide)-grafted surfaces: chain density-dependent multiple mechanisms of action, Langmuir the Acs Journal of Surfaces & Colloids 24 (2008) 1924–1929.

[37] F. Otsuka, A.V. Finn, S.K. Yazdani, M. Nakano, F.D. Kolodgie, R. Virmani, Correction: the importance of the endothelium in atherothrombosis and coronary stenting, Nat. Rev. Cardiol. 9 (2012) 439–453.

[38] M. Hu, H. Chang, H. Zhang, J. Wang, W.-x. Lei, B.-c. Li, K.-f. Ren, J. Ji, Mechanical adaptability of the MMP-responsive film improves the functionality of endothelial cell monolayer, Adv. Healthcare Mater. 6 (2017), 1601410.

[39] Y. Duvault, A. Gagnaire, F. Gardies, N. Jaffrezic-Renault, C. Martelet, D. Morel, J. Serpinet, J.L. Duvault, Physicochemical characterization of covalently bonded alkyl monolayers on silica surfaces, Thin Solid Films 185 (1990) 169–179.

[40] Y. Duvault-Herrera, N. Jaffrezic-Renault, P. Clechet, J. Serpinet, D. Morel, Quantitative study of the hydroxylation and of the chemical grafting of oxidized porous silicon, Colloid. Surface. 50 (1990) 197–206.

[41] Y. Duvault-Herrera, N. Jaffrezic-Renault, D. Morel, J. Serpinet, G. Hollinger, Analytical control of the preparation and the chemical grafting of Si/SiO2 heterostructures. Application to the fabrication of silicon microsensors, Colloids Surf., A 53 (1991) 169–182.

[42] A.Y. Fadeev, T.J. Mccarthy, Trialkylsilane monolayers covalently attached to silicon surfaces: wettability studies indicating that molecular topography contributes to contact angle hysteresis, Langmuir 15 (1999) 3759–3766.